Signatures of Strangeness in Neutron Star Merger Remnants

Krishna Prakash Nunna[1], Sarmistha Banik[1] , and Debarati Chatterjee[2]
[1] Birla Institute of Technology and Science Pilani, Hyderabad Campus, Hyderabad—500078, India; sarmistha.banik@hyderabad.bits-pilani.ac.in
[2] Inter-University Centre for Astronomy and Astrophysics, Pune University Campus, Pune—411007, India

Abstract

Neutron star (NS) mergers provide us with information rich in physics using multimessenger astrophysical observations. One of the probable remnants of such a merger is a differentially rotating hot hypermassive NS. The stability of the merger remnant crucially depends on the underlying equation of state and thus provides a method to probe the nature of dense matter in NSs. In this work, we search for possible signatures of strangeness-containing matter in NS interiors on the secular stability of the merger remnant. We also use recently proposed methods to make a rough estimate of the collapse time of the merger remnant and the threshold mass above which the merger promptly collapses to a black hole.

Unified Astronomy Thesaurus concepts: Neutron star cores (1107); Neutron stars (1108); Relativistic stars (1392)

1. Introduction

Neutron stars (NSs) are compact stellar remnants left behind at the end point of the evolution of massive stars that end in supernova explosions. Typically having masses of 1–2 solar masses ($M_{\rm solar}$) enclosed within a compact radius of only about 10 km, NSs span a wide range of densities. The interior composition of NSs is still a mystery, as the nature of cold and dense matter beyond saturation density is not accessible to terrestrial experiments, and one must resort to theoretical models for their description. While nuclear experiments provide clues about the nature of matter close to the nuclear matter saturation density n_0, heavy-ion collisions provide information about hot and dense matter at a few times n_0. Although such experiments can help to constrain parameters of theoretical models, they must be extrapolated to the regime of low temperatures, higher densities, and finite neutron–proton asymmetry to describe NS matter.

Strangeness is well-established in heavy-ion experiments, where strange particles (hyperons, kaons) have been observed to appear for brief intervals of time. The high densities in NS cores are believed to favor the appearance of strange particles (hyperons, condensates of mesons, or even deconfined quarks), which could then exist as stable constituents due to chemical equilibrium via nonleptonic weak interaction processes. The appearance of such additional degrees of freedom should result in reduction of the pressure and consequently a softer equation of state (EoS) or pressure–density relationship.

The microscopic EoS of dense matter is one of the key ingredients that govern global astrophysical NS observables, such as mass, radii, or moments of inertia. Thus NS observations can help to constrain their internal structure and composition and hence the EoS of dense matter. For example, solving equations of hydrostatic equilibrium, one can obtain the mass and radius of a NS given its EoS. A softer EoS implies a lower pressure at a given density and therefore result in a lower NS mass. This would however be incompatible with the recent observation of large NS masses $\sim 2 M_{\rm solar}$ (Demorest et al. 2010; Antoniadis et al. 2013). There have been many suggestions in the recent past to solve this apparent dilemma (Dexheimer & Schramm 2008; Bednarek et al. 2012; Weissenborn et al. 2012a, 2012b; Yamamoto et al. 2013; Char &

Banik 2014; Lopes & Menezes 2014; Maslov et al. 2015; Oertel et al. 2015; Chatterjee & Vidaña 2016), which revealed the unforeseen role played by interactions among strange particles. The "hyperon puzzle" has been addressed in alternate gravity with geometric terms (Astashenok et al. 2014). In fact, the mass–radius relation of NSs has been discussed consistently in the extended theories of gravity as $f(R)$ gravity (Astashenok et al. 2015; Capozziello et al. 2016; Feola et al. 2020).

Apart from NS masses, there are several other observational signatures of strange matter in NSs. The recently launched Neutron star Interior Composition Explorer mission aims to measure radii with up to 5% precision in the near future, and has already started providing interesting constraints on the dense matter EoS (Raaijmakers et al. 2019). Estimates of NS radii have also been obtained in the recent past from the double pulsar J0737-3039 system (Raithel et al. 2016), which is well constrained from the measurement of its post-Keplerian parameters.

One of the most promising tools that has emerged in the recent past is that of oscillation modes in NSs that emit gravitational waves (GWs). Unlike electromagnetic signals that are related to surface phenomena, GWs can directly probe the interior composition of NSs. Several studies have shown (Chatterjee & Bandyopadhyay 2007, 2008, 2009, 2016) that unstable modes such as r-modes and w-modes contain signatures of strange matter in NS cores that can be extracted from the GW signal when detected. Recently, the detection of GWs from the NS binary merger GW170817 has opened up a new window to the universe. Tidal deformations of the NSs in the binary have been used to provide constraints on the NS radius, and consequently on the dense matter EoS (Abbott et al. 2017a).

The outcome of the NS merger in GW170817 is highly debated, given the uncertainties associated with the detection of the postmerger GWs. Postmerger searches by the LIGO–VIRGO Collaboration did not find evidence for GWs from the remnant (Abbott et al. 2017b, 2019a, 2019b). One possible outcome is a differentially rotating hot hypermassive NS (HMNS) (Baiotti & Rezzolla 2017). The stability of the conjectured hypermassive merger remnant is extremely interesting as it depends crucially on the dense matter EoS as well as the differential rotation velocity profile. Several works in the

literature have explored the equilibrium solutions of differentially rotating NSs (Baumgarte et al. 2000; Gondek-Rosinska et al. 2017).

Recently Bozzola et al. (2018) and Weih et al. (2018) have performed studies of the secular instability in HMNSs and proposed a "quasi-universal" relation between the maximum mass of the remnant and its scaled angular momentum independent of the EoS. The EoSs considered for these works were polytropes, zero-temperature hadronic EoSs, or strange star EoSs. Several recent investigations have also probed the threshold mass beyond which the merger remnant collapses to a black hole and the collapse time. However, their estimates and methodology vary widely (Radice et al. 2018; Gill et al. 2019; Köppel et al. 2019; Lucca & Sagunski 2019). Further, many of the assumptions that go into such calculations (e.g., slow rotation, spindown via electromagnetic radiation only, consistent treatment of thermal contribution in the EoS) must be carefully reconsidered.

In this work, we investigate the role of strangeness in the NS core on the stability of the HMNS merger remnant. We consider only the most realistic solutions of differentially rotating stars that belong to the class "A" (Ansorg et al. 2009), which always have a mass-shedding limit. The signature of the presence of strangeness-containing matter such hyperons and antikaon condensates on the secular instability is investigated, as well as the universality of the proposed relations. We consider differential rotation and include thermal effects, which are crucial properties of a NS merger remnant. We also estimate the threshold mass of the merger remnant for prompt collapse to a black hole and the corresponding collapse time.

The outline of the paper is as follows. In Section 2, we present the formalism, namely the microscopic description and the different EoSs employed in this investigation. We then discuss the numerical scheme employed to obtain the macroscopic NS structure. In Section 3, we obtain the main results of this study. We provide the details of the method used to determine the onset of the secular instability, investigation of the universal relations and an estimation of the collapse time. Section 4 we discuss the main findings of this work and the limitations and scope for further study.

2. Formalism

2.1. EoSs

One of the main goals of this work is to find signatures of strangeness-containing constituents of the NS interior (such as hyperons or antikaon condensates) on the stability of the NS merger remnant. Further, temperatures of 50–100 MeV can be reached in HMNS merger remnants, implying that thermal effects on the EoS cannot be neglected. This may have a significant effect on the composition, favoring the production of hyperons or mesons. A number of different approaches are followed to construct the EoS of cold and ultradense NS matter, as the interaction cannot be described from first principle. In this work, we consider zero-temperature as well as finite-temperature EoSs based on the phenomenological relativistic mean field (RMF) with density-dependent coefficients. It is based on field-theoretical calculations where the constituent baryons interact via meson exchange and the model parameters are fitted to properties of finite nuclei to obtain the bulk properties of nuclear matter. Besides, the meson–baryon couplings are made density dependent, to address the high

density behavior of the EoS. The EoSs used in this work agree with the bounds on the symmetry energy at nuclear density and its derivative with respect to density, set by nuclear experiments. These are unified EoSs in the sense that the same RMF nucleon–nucleon interaction is used in the subsaturation density as well as at high density. Also, they satisfy the $2M_{\mathrm{solar}}$ constraint (Demorest et al. 2010; Antoniadis et al. 2013). Currently, only a few EoSs are available which treat temperature, baryon number density, and electron fraction in a consistent way. These are some of the unified EoSs at a finite temperature that are used for numerical relativity simulations for binary NS mergers.

2.1.1. Zero-temperature EoSs

We consider the following different compositions for the NS core:

(i) pure nucleonic matter (DD2);
(ii) matter with Λ-hyperons (BHB$\Lambda\phi$);
(iii) matter with antikaon condensates (DD2-K^-).

The EoSs used in this work all satisfy the $2M_{\mathrm{solar}}$ constraint (Demorest et al. 2010; Antoniadis et al. 2013). We briefly recapitulate the EoSs below.

(i) Pure nucleonic matter consists of an ensemble of nuclei and interacting nucleons in a nuclear statistical equilibrium. Uniform nuclear matter contains neutrons, protons, and leptons at large densities and is described by an RMF model. Nuclei, on the other hand, are treated as separate particle species, and their masses are taken from nuclear structure calculations which are based on the same nuclear Lagrangian density. For a given number density and temperature the Helmholtz free energy is minimized. Also, within the model the RMF interactions of the nucleons are coupled to the nuclei via chemical equilibrium (Hempel & Schaffner-Bielich 2010). The EoS is denoted as DD2. The thermodynamically consistent description with excluded volume corrections takes care of the transition of the nonuniform nuclear matter phase from nuclei to uniform nuclear matter. Though this guarantees a smooth transition between the nonuniform and uniform parts of the EoS, it may have a 4% uncertainty in the radius calculation, as was emphasized by Fortin et al. (2016). But the determination of maximum mass is not affected by the core–crust matching.

(ii) The NS core density may exceed a few times n_0. At high density, major constituents of matter may have strange particles like Λ hyperons and/or K^- condensates in addition to protons, neutrons, and leptons. The strange particles are never found to coexist with the nuclei as they appear only at high densities. Therefore, we simply use the nonuniform part of the DD2 EoS (Hempel & Schaffner-Bielich 2010) following the standard prescription of minimization of free energy, as developed by one of our authors (Banik et al. 2014). In the presence of hyperon–hyperon interaction via ϕ mesons, the EoS with Λ-hyperons is represented by BHB$\Lambda\phi$ (Banik et al. 2014).

(iii) The antikaons are treated on the same footing as the nucleons following Pons et al. (2000); here the antikaon–baryon couplings are density independent. The

interactions between the constituents of such matter are poorly understood, largely due to the lack of experimental data. We consider an optical potential depth of -140 MeV for the K^- nucleon interaction. This EoS is represented by DD2-K^- (Batra et al. 2018).

2.1.2. Thermal Effects

Newly born protoneutron stars (PNSs) at a finite temperature, as well as hot merger remnants, have been studied elaborately in the literature (Abbott et al. 2017b). One may consider either isothermal or isentropic configurations. Isentropic configurations are quantified by the value of entropy per baryon s in units of the Boltzmann constant k_B. We have seen for a fixed entropy per baryon of $s = 2k_B$ that a NS can shoot a central temperature of 50–100 MeV (Batra et al. 2018). Therefore, it is important to study the role of thermal effects on the stability of the NS. In this study, therefore, we compare two cases:

(i) zero-temperature $(s = 0)$ EoSs as elaborated in Section 2.1.1;
(ii) the same EoSs with thermal effects included $(s = 2k_B)$.

2.2. Numerical Scheme

Differential rotation may support hot HMNS merger remnants against collapse. In order to study the stability of the merger remnants, one must obtain equilibrium NS configurations for the EoSs discussed above (Section 2.1). There are already existing numerical schemes that compute equilibrium solutions of uniform and differentially rotating cold NSs, see, e.g., the numerical library LORENE[3]. Within this scheme, calculations are performed solving general relativistic equations of the hydrostatic equilibrium of rotating, axially symmetric stars. The first attempts toward equilibrium models including thermal effects in uniformly and differentially rotating NSs were introduced by Goussard et al. (1997, 1998) for realistic EoSs. It was shown that for finite temperature, the integrability of the equation of stationary motion requires an isentropic (constant entropy) or isothermal (constant temperature) solution. Rapidly (uniformly) rotating hot NS configurations were also computed within this framework in Marques et al. (2017) for realistic EoSs including hyperons.

In this study we compute equilibrium solutions of hot (isentropic) differentially rotating NSs within the same numerical scheme. Equilibrium equations are solved with Einstein equations, with the assumptions of stationarity, axisymmetry and circularity (the absence of meridional convective currents). An EoS is required to close the system of equations. For a finite temperature, the EoS depends on temperature as well as on the particle number densities. The partial differential Einstein equations are solved using a multidomain spectral method (Bonazzola et al. 1993). An algorithm to construct a rotating equilibrium model numerically in a self-consistent-field method is explicitly described in Bonazzola et al. (1993). We briefly describe it below.

---

[3] www.lorene.obspm.fr

The Schwarzschild metric for a static star gives the following line element:

$$g_{\mu\nu}dx^\mu dx^\nu = -e^{2\nu(r)}dt^2 + \left(1 - \frac{2m(r)}{r}\right)^{-1}dr^2$$
$$+ r^2 d\theta^2 + r^2 \sin^2\theta d\phi^2, \qquad (1)$$

where ν is a metric potential and $m(r)$ is the gravitational mass inside a sphere of radius r. In hydrostatic equilibrium, the structure of a spherically symmetric, static relativistic NS is determined by the Tolman–Oppenheimer–Volkoff (TOV) equations, basically a reformulated Einstein's equation using Equation (1). Given a barotropic EoS (in the form of $\epsilon = \epsilon(n_b)$ and $P = P(n_b)$), the stellar structure can be computed by numerically integrating the TOV equations with suitable boundary conditions.

A rapidly rotating star can be modeled in general relativity within a $3 + 1$D space plus time decomposition of the Einstein equation (Bonazzola et al. 1993), where spacetime is sliced by a family of space-like hypersurfaces Σ_t, labeled by the time coordinate t. The line element can be written as

$$ds^2 = -N^2 dt^2 + \gamma_{ij}(dx^i + \beta^i dt)(dx^j + \beta^j dt). \qquad (2)$$

Here x^i is a coordinate on the hyperspace, N is the proportionality coefficient of two collinear vectors $\boldsymbol{\nabla}t$ and $\boldsymbol{n}$ in $\boldsymbol{n} = -N\boldsymbol{\nabla}t$, called a lapse function, β^i is the shift vector and γ_{ij} the 3-metric on each hypersurface (Bonazzola et al. 1993). Since each hypersurface Σ_t is assumed to be space-like, the components of γ are given in terms of the components of the normal via $\gamma_{\mu\nu} = g_{\mu\nu} + n_\mu n_\nu$.

Spacetime can be stationary and axisymmetric at the same time which implies the existence a of time-like Killing vector field $\boldsymbol{\zeta} = (\partial_t)$ and a space-like Killing field $\boldsymbol{\xi} = \partial_\phi$, respectively. These two commuting Killing vectors imply that we can choose spherical polar coordinates ($x^0 = t$, $x^1 = r$, $x^2 = \phi$, $x^3 = \theta$). Furthermore, for an asymptotically flat spacetime $\beta^r = \beta^\phi = 0$, $\gamma_{r\phi} = \gamma_{\theta\phi} = 0$. Hence, the line element for a rotating star in quasi-isotropic coordinates, which additionally gives $\gamma_{r\theta} = 0$, is given by

$$g_{\alpha\beta}dx^\alpha dx^\beta = -N^2 dt^2 + A^2(dr^2 + r^2 d\theta^2)$$
$$+ B^2 r^2 \sin^2\theta(d\phi - \omega dt)^2, \qquad (3)$$

where N, A, B and ω are four functions of (r, θ). Four Einstein equations for the rotating star involving these four metric potentials reduce to partial differential equations with the matter source terms as well as the gravitational field on their right-hand side.

For a perfect fluid, the stress–energy tensor is given by $T^{\mu\nu} = (\epsilon + P)u^\mu u^\nu + P g^{\mu\nu}$, where ϵ is energy density, P is pressure, both in the fluid frame, and u^μ is the fluid 4-velocity. Due to the circularity hypothesis, the fluid 4-velocity with respect to zero angular momentum observer (ZAMO) can be written as $\boldsymbol{u} = \Gamma(\boldsymbol{n} + \boldsymbol{U})$, where $\boldsymbol{n}$ is the 4-velocity of the ZAMO, $\Gamma = (1 - U^2)^{-1/2}$, and $\boldsymbol{U}$ is the Lorentz factor and 3-velocity of the fluid with respect to ZAMO, respectively. The equations of motion follow from the energy–momentum conservation law, $\nabla^\mu T_{\mu\nu} = 0$, and the baryon number conservation law $\nabla^\mu(n_b u^\mu) = 0$. The first integral of motion is
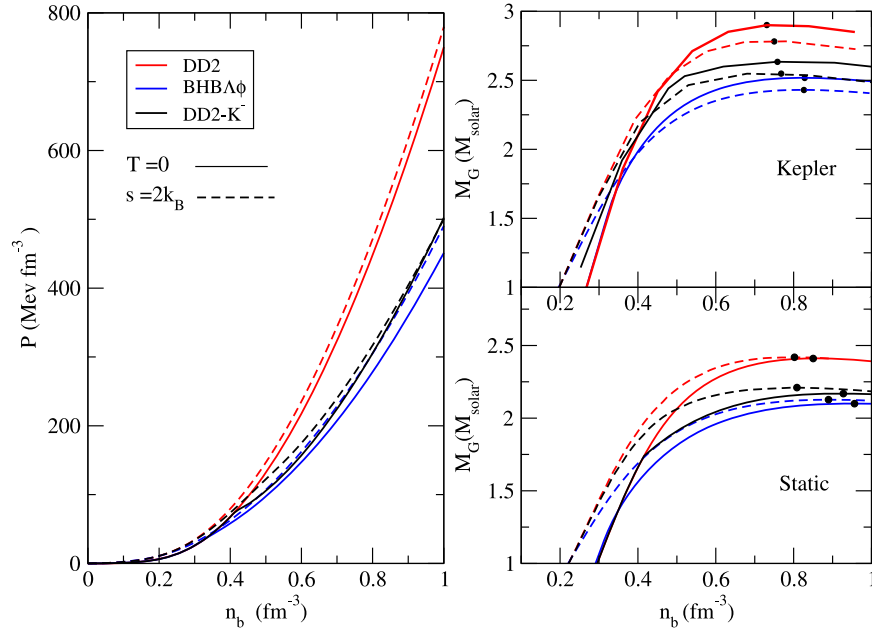
Figure 1. EoSs (left panel) and corresponding gravitational mass–baryon density sequences (static and uniformly rotating Kepler) are plotted in the right panels. Solid lines are used for cold stars ($T = 0$), while dashed lines are used for finite entropy per baryon $s = 2k_B$. See the text for more details.

expressed as

$$\nabla(H + \upsilon - \ln \Gamma) + F(\Omega)\nabla\Omega = 0, \qquad (4)$$

where $H := \ln \frac{h}{m_B}$, m_B being the mean baryon mass: $m_B \simeq 1.66 \times 10^{27}$ kg. For rigid rotation, $\Omega = $ constant and Equation (4) becomes $H + \ln N - \ln \Gamma = $ constant. In the case of differential rotation, $\nabla\Omega \neq 0$ and the first integral of motion is given by

$$H + \upsilon - \ln\Gamma + \int_0^\Omega F(\Omega')d\Omega' = \text{constant.} \qquad (5)$$

For hot stars, the equation of fluid motion is given by

$$\partial_i(H + \upsilon - \ln \Gamma) = \frac{Te^{-H}}{m_B}\partial_i s_B - F\partial_i\Omega. \qquad (6)$$

This numerical method gives a unique solution with the input parameters (H_c, Ω) and a fixed EoS for a rotation law. In order to investigate the role of differential rotation, we employed the usual Komatsu Eriguchi Hachisu (KEH; Komatsu et al. 1989) or j-constant rotation law defined by the velocity profile:

$$F(\Omega) = R_0^2 \, (\Omega_c - \Omega), \qquad (7)$$

where Ω_c is the central angular frequency and R_0 is a free parameter with dimensions of length that determines the degree of differential rotation (Baumgarte et al. 2000). We consider the dimensionless parameter $a = R_e/R_0$, where R_e is the equatorial NS radius. Thus the limit of uniform rotation is obtained when $a \to 0$ and increasing a denotes increasing degree of differential rotation. The advantage of the j-constant law is that it approximately reproduces the rotation profile obtained in 2D simulations, and is a simple law, with the minimum number of free parameters. Although the j-constant rotation law is the most widely used, alternative rotation laws have been discussed in the literature (Uryu et al. 2017; Bozzola et al. 2018) and should be investigated. However, such a task is

beyond the scope of this paper, and we leave it for a future study. It should be noted that the previously obtained stationary state equilibrium solutions for hot differentially rotating PNSs were also investigated by Goussard et al. (1997) using the j-constant rotation law.

3. Results

The EoSs discussed in Section 2.1 and the corresponding mass–density relations for the nonrotating as well as the mass-shedding cases are shown in Figure 1. In the left panel pressure P (in MeV fm^{-3}) is plotted against the baryon number density n_b (in fm^{-3}) for (i) pure nucleonic matter, (ii) hyperons, and (iii) antikaon condensates denoted by DD2, BHB$\Lambda\phi$, and DD2-K^- respectively. The DD2 EoS is the stiffest of the three, which softens with the advent of extra degrees of freedom in the form of strange particles, K^- condensates, and Λ-hyperons. Again, the EoSs are stiffer for stars with finite entropy per baryon compared to the cold ones for all the three cases, the difference arising from the thermal contribution to the pressure. We use solid lines for $T = 0$ and dashed ones for stars at $s = 2k_B$.

Solving the TOV equations of a relativistic hydrostatic equilibrium, we obtain the macroscopic structure properties (mass and radius) of the NS. The solutions for the static star corresponding to the different EoSs are plotted in the lower-right panel of Figure 1. As expected, the strange EoS yields a lower maximum mass star compared to that of the DD2 EoS. A stiffer EoS can support larger mass. However, all the sets of EoSs yield maximum mass above the observational $2M_{\rm solar}$ limit (Demorest et al. 2010; Antoniadis et al. 2013).

Let us follow a NS with similar compositions. Between a cold ($T = 0$) and hot ($s = 2k_B$) EoS, the latter being stiffer can support a static star of larger mass, compared to its cold counterpart. However, this trend is reversed for the mass-shedding sequences. We plot the mass of sequences of uniformly rotating stars at the Keplerian limit in the upper right panel of Figure 1. The maximum masses for the Keplerian

Table 1
Turning Points for Stars Rotating Differentially ($a = 0.2$) for a Zero-temperature DD2 EoS

			DD2, $T = 0$ ($s = 2k_{\rm B}$)			
J	ρ_c	M_G	f_c	r_p/r_e	$R_{\rm circ}$	T/W
7.36(5.39)	9.86(10.11)	3.08(2.86)	1820.78(1532.18)	0.48(0.60)	16.51(16.12)	0.167(0.119)
4.38	10.66(9.91)	2.72(2.74)	1510.12(1387.25)	0.74(0.70)	13.39(14.97)	0.095(0.093)
3.68	10.88(10.32)	2.64(2.66)	1367.54(1272.82)	0.79(0.76)	12.29(14.30)	0.075(0.074)
3.33	10.88(10.53)	2.61(2.62)	1278.70(1191.50)	0.82(0.80)	12.85(13.99)	0.065(0.063)
2.94	11.09(10.53)	2.57(2.58)	1176.64(1101.74)	0.85(0.82)	12.64(13.79)	0.054(0.053)
2.33	11.32(10.75)	2.51(2.53)	983.05(925.88)	0.89(0.88)	12.37(13.42)	0.036(0.036)
1.54	11.77(10.97)	2.46(2.47)	693.18(652.35)	0.95(0.94)	12.0(13.07)	0.017(0.017)
5.91(4.82)	10.05(10.11)	2.90(2.79)	1537.86(1354.41)	0.68(0.58)	13.74(16.92)	0.13(0.10)
0(0)	11.77(11.43)	2.41(2.42)	0(0)	1(1)	11.86(12.72)	0(0)

Note. The values in parentheses are for $s = 2k_{\rm B}$. Among them, the topmost row is for stars spinning at the Kepler frequency. The last two rows are for a uniformly rotating star at Keplerian frequency and for a static star, respectively. (See the text for details.)

sequences increase by ∼20%–23% more than their static ones for the cold stars, whereas for the stars with $s = 2k_{\rm B}$ the differences are ∼12%–15%. The values of maximum mass and other relevant properties are given in Table 1. The thermal pressure contribution can sustain a heavier NS. But it is evident from the table that the Keplerian frequency for a hot NS is not as high as that of the cold star. Hence the difference in maximum mass is lower for hotter stars.

3.1. Onset of Secular Instability

The onset of the secular instability is determined by the "turning point" (TP) criterion, i.e., the maximum of the gravitational masses as a function of central density (Friedman et al. 1988). The TP criterion for secular stability in hot rigidly rotating stars was obtained (Goussard et al. 1997; Marques et al. 2017) for isentropic (or isothermal) solutions. Considering sequences of differentially rotating equilibrium models using the j-constant law, it was shown that a stability criterion for differentially rotating NSs exists similar to the one for their uniformly rotating counterparts (Bozzola et al. 2018; Weih et al. 2018). The onset of dynamical instability for differentially rotating stars is marked by the neutral-stability line (where the eigenfrequency of the fundamental mode of oscillation vanishes). The neutral-stability and TP curves coincide for nonrotating NSs, but their difference grows with increasing angular momentum. Along a sequence of constant angular momentum, dynamical instability sets in for central rest-mass densities slightly lower than that of secular instability at the TP.

In order to investigate the effect of the NS core composition on the stability of the NS merger remnant, one must construct relativistic equilibrium sequences and calculate the extra mass supported by the rotating star compared to the static star for the EoSs considered. However, it has already been shown that sequences at constant rotation frequency do not allow one to distinguish between stable and unstable solutions (Marques et al. 2017), but rather sequences of constant angular momentum must be compared. We therefore generate equilibrium sequences at constant angular momentum for a given degree of differential rotation a.

In Figure 2, we display gravitational mass M_G (in solar masses) as a function of central energy density ρ_c (in units of $\rho_{\rm nuc}c^2$, where $\rho_{\rm nuc} = 1.66 \times 10^{17}$ kg m^{-3}) for the nucleonic DD2 EoS. The nonrotating limit is denoted by the red "static" curves while the mass-shedding limit is denoted by black
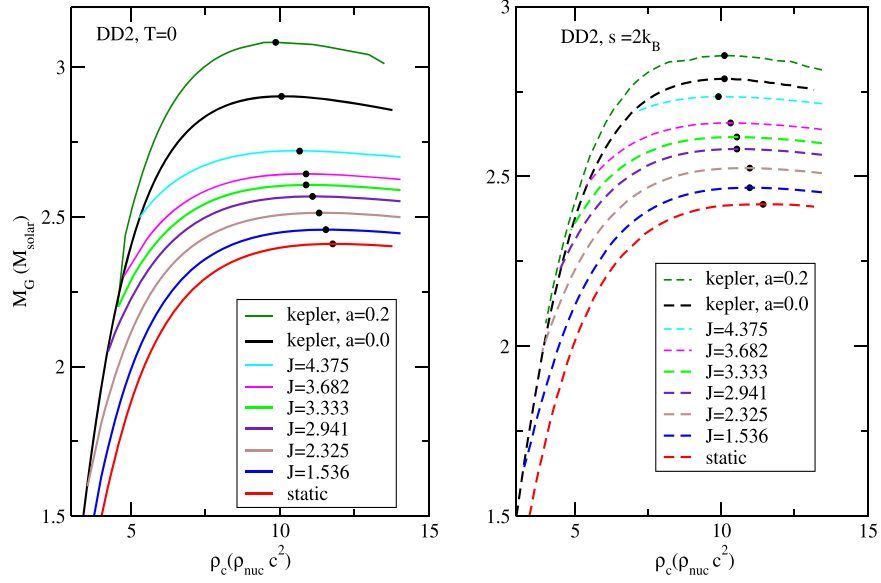
"kepler" curves for uniformly rotating NSs. Also plotted (in color) are constant angular momentum sequences (labeled by their angular momentum values "J") for a given degree of differential rotation ($a = 0.2$). In order to study the thermal effects, different values of entropy are considered, $T = 0$ in the left panel and $s = 2k_{\rm B}$ in the right panel.

In Figure 3, we show the static and mass-shedding limit for uniformly rotating equilibrium sequences for the BHBΛϕ EoS. Constant angular momentum sequences for the differential rotation parameter $a = 0.2$ are also included in between the static and "kepler" sequences. The left panel displays the zero-temperature case while the right panel includes thermal effects ($s = 2k_{\rm B}$). As before, the different parameters are summarized in Table 2.

In Tables 1–3, we study the TP criterion, considering DD2, BHBΛϕ, or DD2-K^- EoSs for $s = 0$ and $s = 2k_{\rm B}$, respectively. The columns represent, respectively, the angular momentum J (in $GM_{\rm solar}^2/c$), central energy density ρ_c (in $\rho_{\rm nuc}c^2$), gravitational mass M_G (in $M_{\rm solar}$), central frequency f_c in hertz, ratio of polar and equatorial radii r_p/r_e, ratio of central and equatorial angular frequencies Ω_c/Ω_e, circumferential radius $R_{\rm circ}$ (in kilometers) and the ratio of kinetic to gravitational energy T/W.

3.2. Universal Relations

In this work, we investigate whether the presence of strangeness affects the universality of the relations proposed recently (Bozzola et al. 2018; Weih et al. 2018). In Figure 4, the maximum or TP masses of differentially rotating sequences $M_{\rm max,dr}$ for a given degree of differential rotation ($a = 0.2$) normalized to the corresponding TOV mass $M_{\rm TOV}$ is plotted as a function of normalized dimensionless angular momentum $j/j_{\rm max,0}$ for the different EoSs discussed in Section 2.1. Here $j = J/M^2$ while $j_{\rm max,0}$ is the maximum value of j at the mass-shedding limit for a uniformly rotating NS. It is evident from the figure that thermal effects spoil the universality of the relations. This is interesting because the HMNS merger remnant is hot (temperature ∼80 MeV) and hence thermal effects cannot be ignored. However we find that the behavior of the cold and hot EoSs individually do not vary qualitatively. In both cases, for differential rotation $a = 0.2$, the curves are independent of the different EoSs considered in this work. So we fit the curves for the cold and hot EoSs with a simple

Figure 2. Equilibrium sequences for nucleonic EoS for nonrotating (red "static" curve) and mass-shedding or "kepler" limits of uniformly rotating NSs (black curve) and differentially rotating NSs at the degree of differential rotation $a = 0.2$ (dark-green curve). Also plotted (in color) are constant angular momentum sequences (labeled by their "J" values) for $a = 0.2$. The left panel is for $T = 0$, the right panel is for entropy per baryon $s = 2k_B$. The black dots denote the TPs.
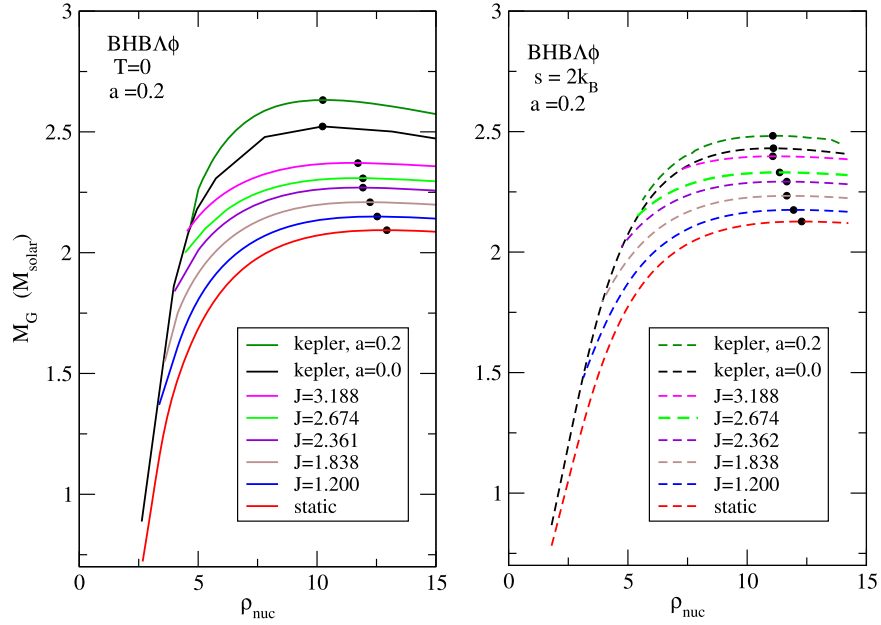
Figure 3. Same as Figure 2, but for BHB$\Lambda\phi$ EoS.

Table 2
Turning Points for the Zero-temperature BHB$\Lambda\phi$ EoS

			BHB$\Lambda\phi$, $T = 0$ ($s = 2k_B$)			
J	ρ_c	M_G	f_c	r_p/r_e	R_{circ}	T/W
5.02(3.82)	10.24(11.08)	2.63(2.48)	1583.14(1297.45)	0.51(0.54)	16.67(17.48)	0.143(0.103)
3.19	11.72(11.08)	2.38(2.40)	1395.82(1303.96)	0.73(0.69)	13.29(14.95)	0.087(0.832)
2.67	11.92(11.36)	2.31(2.33)	1272.70(1192.95)	0.79(0.76)	12.85(14.21)	0.069(0.066)
2.36	11.63(11.66)	2.27(2.29)	1174.38(1111.55)	0.82(0.80)	12.63(13.81)	0.057(0.055)
1.84	12.22(11.66)	2.21(2.23)	988.34(927.662)	0.88(0.86)	12.26(13.37)	0.039(0.037)
1.20	12.53(11.95)	2.15(2.18)	698.29(656.40)	0.94(0.93)	11.89(12.91)	0.019(0.017)
4.28(3.44)	10.24(11.10)	2.52(2.43)	1413.10(1277.04)	0.56(0.58)	15.93(16.88)	0.122(0.091)
0(0)	12.84(12.26)	2.10(2.13)	0(0)	1(1)	11.52(12.5)	0(0)

Note. The values in parentheses are for $s = 2k_B$ (see the text for details).

Table 3
Turning Points for Zero-temperature DD2-K^- EoS

			DD2-K^-, $T = 0$ ($s = 2k_B$)			
J	ρ_c	M_G	f_c	r_p/r_e	R_{circ}	T/W
5.54(4.33)	9.65(9.59)	2.74(2.61)	1586.44(1356.46)	0.50(0.54)	16.94(18.15)	0.149 (0.109)
3.02	11.41(9.86)	2.40(2.44)	1307.14(1140.28)	0.77(0.75)	13.09(14.94)	0.075(0.07)
2.89	11.41(10.13)	2.39(2.42)	1273.24(1122.21)	0.79(0.77)	13.00(14.76)	0.070(0.066)
1.71	11.96(10.41)	2.26(2.30)	882.16(773.57)	0.90(0.90)	12.23(13.75)	0.031(0.029)
1.13	11.94(10.98)	2.21(2.25)	620.09(550.58)	0.95(0.95)	11.94(13.31)	0.015(0.014)
4.65(3.84)	10.13(9.60)	2.62(2.55)	1429.12(1210.26)	0.56(0.58)	16.08(17.79)	0.126(0.095)
0(0)	12.53(10.98)	2.17(2.21)	0(0)	1(1)	11.69(13.07)	0(0)

Note. The values in parentheses are for $s = 2k_B$ (see text for details).
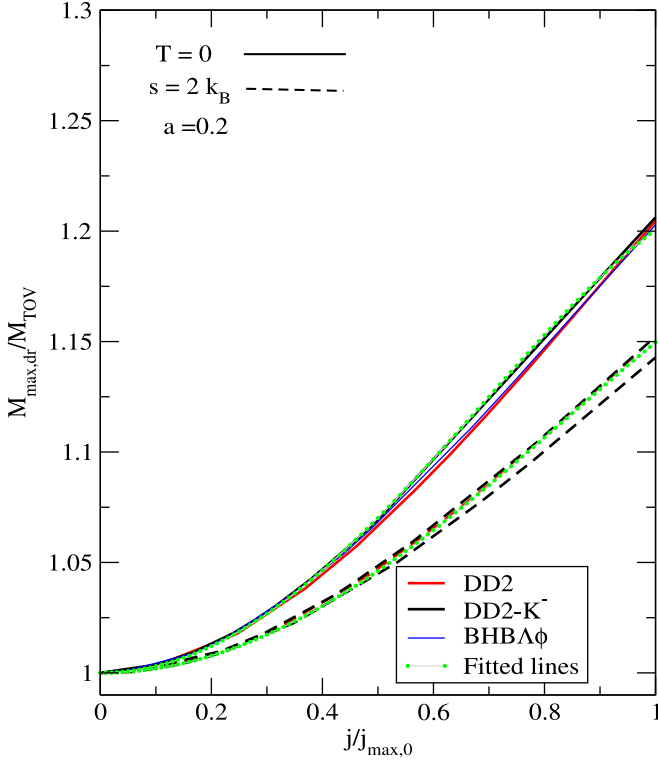
Figure 4. Maximum or TP mass normalized to TOV mass of differentially rotating sequences for a degree of differential rotation ($a = 0.2$) as a function of normalized dimensionless angular momentum for different EoSs (see text for details).

polynomial function of the form

$$\frac{M_{max,dr}}{M_{TOV}} = 1 + b_1(a)\left(\frac{j}{j_{max}}\right)^2 + b_2(a)\left(\frac{j}{j_{max}}\right)^4, \quad (8)$$

where the coefficients are found to be $b_1 = 0.30735(0.1964)$ and $b_2 = -0.10671(-0.04671)$ for cold(hot) stars, respectively, for the differential rotation parameter $a = 0.2$. For comparison with previous works (Weih et al. 2018), in Figure 5 we show the maximum masses of differentially rotating sequences $M_{max,dr}$ for differential rotation $a = 0.2$, but this time as a function of the normalized dimensional angular momentum $j/j_{max,a}$ for the mass-shedding limit of differentially rotating stars. It is obvious that in this case, the maximum masses at $j = j_{max,a}$ are higher, but the spread of the curves for different EoSs is also larger.

We have just established that irrespective of the EoS, there are two families of curves of hot ($s = 2$) and cold ($T = 0$) stars for a differentially rotating star with $a = 0.2$. We now investigate whether this holds true for other values of differential rotation a. In Figure 6, the maximum or TP masses normalized to the corresponding TOV mass of differentially rotating sequences for different degrees of differential rotation a are plotted as a function of the normalized dimensionless angular momentum $j/j_{max,0}$ for one representative EoS, DD2, for the two families $T = 0$ and $s = 2$. We find that curves in the two families coincide for all the values of a considered ($0 < a < 1$). This also holds true for the other EoSs considered in this study (BHB$\Lambda\phi$ and DD2-K^-). Therefore, the fit relation proposed in Equation (8) also holds true for other values of a independent of the EoSs considered in this work.

In order to determine the absolute maximum mass of a hot or a cold differentially rotating star, one needs to compute equilibrium configurations with increasing j until the mass-shedding limit for each a is reached. If the fit relation of $j_{max,a}/j_{max,0}$ with a is known (see Figure 7), then one may determine the absolute maximum mass using the universal fit function in Equation (8). However, it is numerically very challenging to generate Kepler sequences for large values of differential rotation. In Figure 7, we could obtain mass-shedding configurations up to differential rotation $a = 0.3$ for both hot and cold stars, but for higher a the uncertainties are large. For the equilibrium configurations we could obtain (see Figure 6), the maximum mass obtained was $M_{max}/M_{TOV} = 1.23$ (1.19) for the cold (hot) star. The value corresponding to the cold star is lower than the value 1.54 ± 0.05 obtained by Weih et al. (2018) and comparable to the value of 1.2 from Bozzola et al. (2018).

3.3. Collapse Time of the Merger Remnant

The value of the total progenitor mass of the NS binary in GW170817 is derived to be 2.74 $M_\odot$. The mass of the remnant of the BNS merger has been estimated to be ~2.7–2.8 $M_\odot$. There are various possible outcomes of a NS merger that have been conjectured (Ravi & Lasky 2014):

(i) a uniformly rotating stable NS (if the progenitor mass $M_P \leqslant M_{TOV}$). If the EoS is stiff enough, this scenario could be possible (Ai et al. 2018);

(ii) a uniformly rotating supramassive NS (if $M_P > M_{TOV}$). In this case the remnant survives collapse as long as there is enough centrifugal support from rotation;
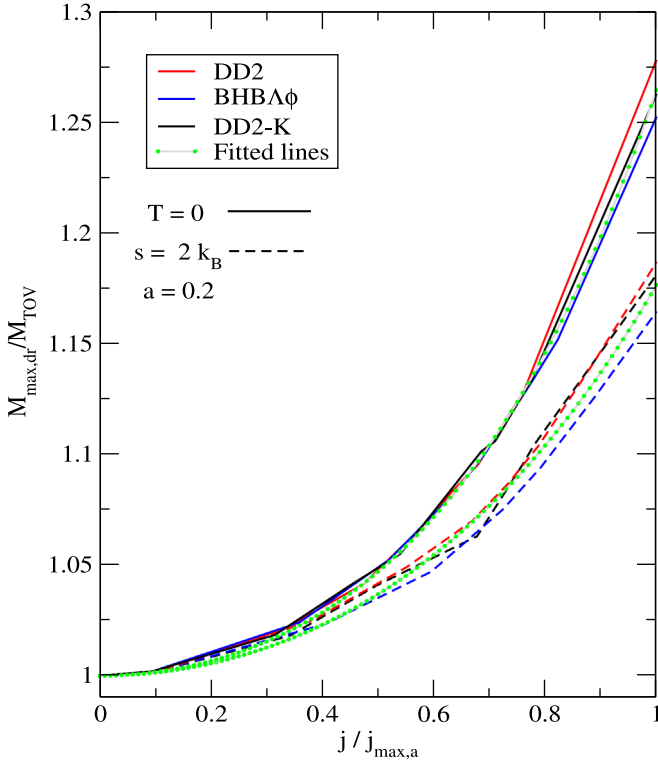
Figure 5. Maximum or TP mass normalized to TOV mass of differentially rotating sequences ($a = 0.2$) as in Figure 4, angular momentum is, however, normalized by the corresponding differential rotation value for different EoSs.
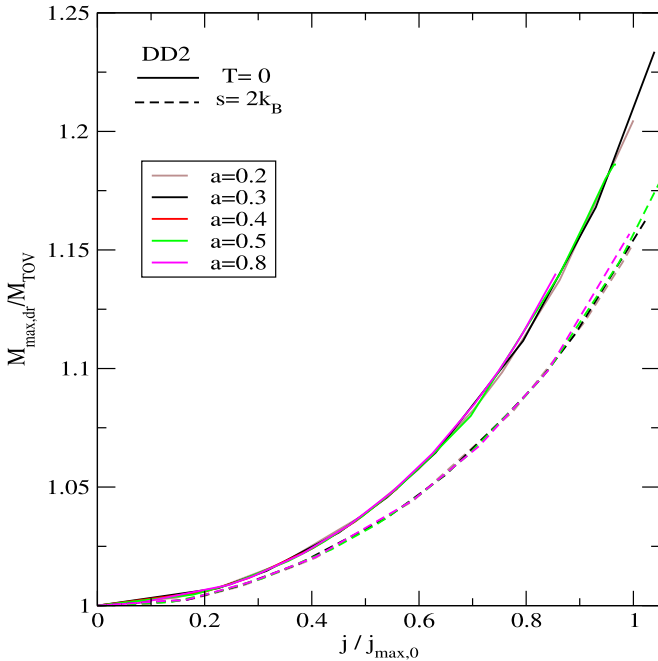
Figure 6. Maximum or TP mass normalized to TOV mass of differentially rotating sequences for the DD2 EoS for different degrees of differential rotation a as a function of normalized dimensionless angular momentum of uniformly rotating stars (see text for details).

(iii) a hot differentially rotating HMNS (if M_P is greater than the maximum mass supported by uniform rotation).

A dynamically unstable HMNS merger remnant may be supported against collapse by the strong differential rotation
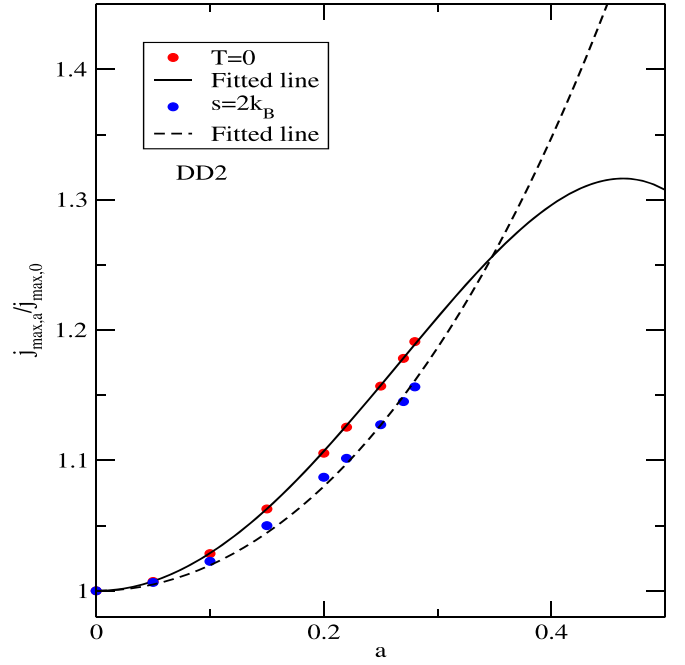
Figure 7. Ratio of normalized angular momenta for differentially rotating stars to uniformly rotating stars as a function of differential rotation a for the DD2 EoS (see text for details) for hot stars (red circles) and cold stars (blue circles). The fit to these curves is also shown.

and thermal pressure. If the remnant is strongly magnetized (protomagnetars with $B \sim 10^{15}$ G), differential rotation is damped on the Alfvén timescale ($\gtrsim 100$ ms). Subsequent dissipation of the differential rotation and thermal energy by neutrinos (on the neutrino cooling timescale $\sim$s) may result in a collapse of the HMNS merger remnant to a black hole on a timescale $\simeq 1$ s, depending on the total mass, mass ratio, and EoS of the NS binary. This may correspond to the 1.74 s delay between the merger chirp signal and GRB170817A. The collapse time of the remnant has important implications for multimessenger astronomy (electromagnetic, GW, or neutrino signal). The observation of the blue kilonova and La-rich ejecta associated with GW170817 may indicate the formation of HMNSs (Tong et al. 2018). In the future, GW observations from the postmerger remnant with the third generation of interferometers (LIGO India, Kagra, Einstein Telescope) might help to constrain the EoS of merger remnants.

Numerical simulations indicate that the HMNS is formed after the merger with a rapidly rotating highly nonaxisymmetric bar-like structure (Gill et al. 2019). This should result in a time-varying quadrupole moment, with strong emission of GW dominating the spindown. Once the differential rotation is damped, the HMNS may become a supramassive NS configuration, with a spindown dominated by magnetic braking. If the merger remnant is a supramassive NS, the large rotational energy released in the isotropic MHD wind produces a large spindown luminosity $L_{SD} > 10^{42}$ erg s^{-1}. But the observed bolometric luminosity is lower than 10^{42} erg s^{-1} and no afterglow emission has been seen. Hence the possibility of a supramassive NS remnant may be ruled out. Thus the only possibility to be considered would be that of a HMNS merger remnant.

As we are interested in the stability of the HMNS merger remnant, we would like to make an estimate of the collapse time for the EoSs investigated in this work. However, the

collapse time estimates and calculations that exist in the literature vary widely in their formalism and predictions and are far from reaching a consensus (Radice et al. 2018; Gill et al. 2019; Köppel et al. 2019; Lucca & Sagunski 2019). We follow some of the recent suggested methods to obtain estimates of the collapse time and the threshold mass for prompt collapse for the EoSs considered in this work.

Assuming slow rotation and spindown of a possible supramassive NS merger remnant via electromagnetic radiation, (Lasky et al. 2014; Ravi & Lasky 2014) analytically obtained estimates for collapse time using observations of short gamma-ray bursts by Swift. However, as observational evidence (Gill et al. 2019) now points to the fact that the remnant of the merger GW170817 may be a rapidly differentially rotating HMNS spinning down via gravitational radiation rather than a supramassive NS, the validity of such relations become questionable.

In the recent work of Köppel et al. (2019), collapse times were computed using hydrodynamical simulations for five zero-temperature EoSs, adding a "thermal contribution" via an ideal-fluid EoS (Rezzolla & Zanotti 2013). But this approach of a "hybrid EoS" is known to be non-self-consistent. Among the EoSs considered were DD2 and BHB$\Lambda\phi$, which we have also employed in this investigation for both zero temperature ($s = 0$) and finite temperature ($s = 2k_B$). The calculation of threshold mass M_{th} above which the merger remnant promptly collapses to form a black hole was also explored in this work. Extending a previously proposed linear EoS-independent universal relation (Bauswein et al. 2013, 2017)

$$M_{th}/M_{TOV} = 3.38\, C_{TOV} + 2.43$$

where the compactness $C_{TOV} = M_{TOV}/R_{TOV}$, they suggested the following nonlinear fit formula

$$M_{th} = a - \frac{b}{1 - c\, C_{TOV}},$$

where $b = 1.01$, $c = 1.34$, and $a = \frac{2b}{2-c}$, taking into account the expected black hole limit $M_{th}/M_{TOV} \to 0$ for $C_{TOV} \to 1/2$.

Recently, the results from simulations (see, e.g., Köppel et al. 2019) and observations (e.g., Lasky et al. 2014; Ravi & Lasky 2014) were combined to derive a radius-independent fit relation between the initial mass of the single NSs M_{NS} and the collapse time t_{coll} (Lucca & Sagunski 2019):

$$\log(t_{coll}) = e_0 + e_1 \log\left(\frac{M_{NS}}{M_{TOV}}\right), \tag{9}$$

where $e_0 = -5.45 \pm 0.40$ and $e_1 = -38.9 \pm 1.7$. The robustness of such a relation was tested and proposed as a useful tool to constrain NS EoSs (Lucca & Sagunski 2019). The BHB$\Lambda\phi$ ($s = 0$) EoS was also one of the EoSs considered.

In order to compare with the results discussed above, we consider the same values of initial data as in Köppel et al. (2019), namely the initial masses $M_{NS} = 1.53$, 1.55, and 1.57 M_{solar} for the DD2 EoS and 1.62, 1.63 and 1.65 M_{solar} for the BHB$\Lambda\phi$ EoS. Using the formula for M_{th} suggested in Köppel et al. (2019), we calculated the threshold mass for prompt collapse in units of M_{TOV}. The results for the $s = 0$ as well as $s = 2$ cases are summarized in Table 4. For comparison with previous works, we also provide the maximum static mass M_{TOV}, corresponding radius R_{TOV}, compactness C_{TOV}, and the

freefall timescale

$$\tau_{TOV} = \frac{\pi}{2}\sqrt{\frac{R_{TOV}^3}{2M_{TOV}}}. \tag{10}$$

We then apply Equation (9) to calculate collapse times t_{coll} for comparison with the results of Lucca & Sagunski (2019). The estimated values of t_{coll} (taking only the mean values for the fit coefficients e_0 and e_1) corresponding to the different M_{NS} are provided in Table 4.

4. Discussions

Since the detection of GWs from the NS binary merger event GW170817, the fate of the binary remnant remains a mystery. As no evidence of a remnant has yet been found from postmerger searches by the LIGO–VIRGO Collaboration, one may study the different possibilities theoretically. One likely outcome of the merger is a metastable differentially rotating HMNS. As the stability (dynamical and secular) and time of subsequent collapse of the remnant depend on its rotation profile and its interior composition, it opens up the possibility to constrain the dense matter EoS using its stability analysis.

In this work, we explored the onset of secular instability for different EoSs with and without strangeness. Using the TP criterion, we investigated the maximum mass that may be supported by differential rotation and thermal effects for the different EoSs considered. We found that inclusion of thermal effects reduced the maximum mass of the differentially rotating configurations. This is interesting as the hypermassive remnant is conjectured to be hot, and hence thermal effects cannot be neglected. When studying the maximum mass supported by an HMNS remnant, previous works considered cold stars or a very restricted sets of EoSs, e.g., polytropic EoSs or only nucleonic matter. With realistic EoSs including hyperonic and kaonic degrees of freedom we investigated the influence of these new degrees of freedom on the maximum supported mass.

We found that the maximum mass obtained depends both on the EoS and the degree of differential rotation. In order to calculate the highest possible value of the maximum mass, we followed the method for obtaining a "universal relation" proposed by Baiotti & Rezzolla (2017) for uniform rotation, extended for the case of differential rotation by Bozzola et al. (2018) and Weih et al. (2018). However for the EoSs considered, we found the universal relation to be practically independent of the EoS and the degree of differential rotation. The highest mass obtained in our analysis was $M_{max} = 1.23$ M_{TOV} for cold NSs and 1.19 M_{TOV} for hot NSs.

We further investigated the effect of strangeness on the collapse time of the merger remnant. We considered the scenario in which the HMNS merger remnant rapidly loses angular momentum due to loss of energy by GW emission and collapses to a black hole before the Alfvén timescale, i.e., before the differential rotation is damped by magnetic dissipation. This scenario is currently favored by the combined multimessenger astrophysical observations (Gill et al. 2019). We estimated the collapse time and threshold mass for prompt collapse for the EoSs with and without strangeness, using recently proposed fit formulas (Köppel et al. 2019; Lucca & Sagunski 2019) obtained using observations of short gamma-ray bursts (Lasky et al. 2014) and hydrodynamical simulations (Köppel et al. 2019).

Table 4
The Estimated Values of t_{coll} (Taking Only the Mean Values for the Fit Coefficients e_0 and e_1) Corresponding to the Different M_{NS}.

EoS	M_{NS} (M_{solar})	s (k_B)	M_{TOV} (M_{solar})	R_{TOV} (km)	C_{TOV}	t_{coll} (ms)	τ_{TOV} (μs)	M_{th} (M_{TOV})
DD2	1.62	0	2.41	11.86	0.30	18.2	80.2	1.37
	1.63					14.29		
	1.65					8.89		
DD2	1.62	2	2.418	12.72	0.28	20.72	88.9	1.44
	1.63					16.31		
	1.65					10.15		
BHB$\Lambda\phi$	1.53	0	2.10	11.52	0.27	0.79	82.26	1.48
	1.55					0.48		
	1.57					0.29		
BHB$\Lambda\phi$	1.53	2	2.127	12.5	0.25	1.31	92.36	1.54
	1.55					0.79		
	1.57					0.48		

Note. For each EoS, we provide the maximum static mass, corresponding radius, compactness, freefall timescale (Köppel et al. 2019), threshold mass for prompt collapse (Köppel et al. 2019), and collapse time (Lucca & Sagunski 2019). See text for more details.

Postmerger multimessenger searches may be able to answer the question about the fate of the merger remnant in GW170817 by ruling out some of the proposed scenarios. Future GW events from other NS mergers along with multimessenger observations will provide further information about the stability of NS merger remnants as well as the dense matter EoS. An exciting journey in multimessenger astronomy has only just begun.

ORCID iDs

Sarmistha Banik ⓘ https://orcid.org/0000-0003-0221-3651

References

Abbott, B. P., LIGO Scientific Collaboration, Virgo Collaboration, et al. 2017a, PhRvL, 119, 161101
Abbott, B. P., Abbott, R., Abbott, T.D., et al. 2017b, ApJL, 851, L16
Abbott, B. P., Abbott, R., Abbott, T.D., et al. 2019a, ApJ, 875, 160
Abbott, B. P., Abbott, R., Abbott, T.D., et al. 2019b, PhRvX, 9, 011001
Ai, S., Gao, H., Dai, Z.-G., et al. 2018, ApJ, 860, 57
Ansorg, M., Gondek-Rosińska, D., & Villain, L. 2009, MNRAS, 396, 2359
Antoniadis, J., Freire, P.C.C., Wex, N., et al. 2013, Sci, 340, 448
Astashenok, A. V., Capozziello, S., Odintsov, S.D., et al. 2014, PhRvD, 89, 103509
Astashenok, A. V., & Odintsov, S.D. 2015, JCAP, 2015, 001
Baiotti, L., & Rezzolla, L. 2017, RPPh, 80, 096901
Banik, S., Hempel, M., & Bandyopadhyay, D. 2014, ApJS, 214, 22
Batra, N. D., Nunna, K. P., & Banik, S. 2018, PhRvC, 98, 035801
Baumgarte, T. W., Shapiro, S. L., & Shibata, M. 2000, ApJL, 528, L29
Bauswein, A., Baumgarte, T. W., & Janka, H.-T. 2013, PhRvL, 111, 131101
Bauswein, A., Just, O., Janka, H.-T., & Stergioulas, N. 2017, ApJL, 850, L34
Bednarek, I., Zdunik, J.L., Bejger, M., Manka, R., et al. 2012, A&A, 157, 543
Bonazzola, S., Gourgoulhon, E., Salgado, M., & Marck, J. 1993, A&A, 278, 421
Bozzola, G., Stergioulas, N., & Bauswein, A. 2018, MNRAS, 474, 3557
Capozziello, S., Laurentis, M.D., Farinelli, R., & Odintsov, S.D. 2016, PhRvD, 93, 023501
Char, P., & Banik, S. 2014, PhRvC, 90, 015801
Chatterjee, D., & Bandyopadhyay, D. 2007, Ap&SS, 308, 451
Chatterjee, D., & Bandyopadhyay, D. 2008, JPhG, 35, 104078
Chatterjee, D., & Bandyopadhyay, D. 2009, PhRvD, 80, 023011
Chatterjee, D., & Bandyopadhyay, D. 2016, PhRvD, 74, 023003
Chatterjee, D., & Vidaña, I. 2016, EPJA, 52, 29
Demorest, P. B., Pennucci, T., Ransom, S., Roberts, M.S.E., & Hessels, J.W.T. 2010, Natur, 467, 1081
Dexheimer, V., & Schramm, S. 2008, ApJ, 683, 943
Feola, P., Forteza, X.J., Capozziello, S., Cianci, R., & Vignolo, S 2020, PhRvD, 101, 044037
Fortin, M., Providência, C., Raduta, A.R., et al. 2016, PhRvC, 94, 035804
Friedman, J. L., Ipser, J. R., & Sorkin, R. D. 1988, ApJ, 325, 722
Gill, R., Nathanail, A., & Rezzolla, L. 2019, ApJ, 876, 139
Gondek-Rosinska, D., Kowalska, I., Villain, L., Ansorg, M., & Kucaba, M. 2017, ApJ, 837, 58
Goussard, J.-O., Haensel, P., & Zdunik, J. L. 1997, A&A, 321, 822
Goussard, J.-O., Haensel, P., & Zdunik, J. L. 1998, A&A, 330, 1005
Hempel, M., & Schaffner-Bielich, J. 2010, NuPhA, 837, 210
Komatsu, H., Eriguchi, Y., & Hachisu, I. 1989, MNRAS, 237, 355
Köppel, S., Bovard, L., & Rezzolla, L. 2019, ApJL, 872, L16
Lasky, P. D., Haskell, B., Ravi, V., Howell, E. J., & Coward, D. M. 2014, PhRvD, 89, 047302
Lopes, L. L., & Menezes, D. P. 2014, PhRvC, 89, 025805
Lucca, M., & Sagunski, L. 2019, arXiv:1909.08631
Marques, M., Oertel, M., Hempel, M., & Novak, J. 2017, PhRvC, 96, 045806
Maslov, K. A., Kolomeitsev, E. E., & Voskresensky, D. N. 2015, PhLB, 748, 369
Metzger, B. D., Thompson, T. A., & Quataert, E. 2018, ApJ, 856, 101
Oertel, M., Providência, C., Gulminelli, F., & Raduta, Ad. R. 2015, JPhG, 42, 075202
Pons, J. A., Ellis, P.J., Prakash, M., & Lattimer, J.M. 2000, PhRvC, 62, 035803
Raajimakers, G., Greif, S.K., Riley, T.E., et al. 2019, ApJL, 893, L21
Radice, D., Perego, A., Hotokezaka, K., et al. 2018, ApJ, 869, 130
Raithel, C. A., Özel, F., & Psaltis, D. 2016, PhRvC, 93, 032801
Ravi, V., & Lasky, P. D. 2014, MNRAS, 441, 2433
Rezzolla, L., & Zanotti, O. 2013, Relativistic Hydrodynamics (Oxford: Oxford Univ. Press)
Tong, H., Yu, C., & Huang, L. 2018, RAA, 18, 067
Uryu, K., Tsokaros, A., Baiotti, L., et al. 2017, PhRvD, 96, 103011
Weih, L. R., Most, E. R., & Rezzolla, L. 2018, MNRAS, 473, L128
Weissenborn, S., Chatterjee, D., & Schaffner-Bielich, J. 2012a, NuPhA, 881, 62
Weissenborn, S., Chatterjee, D., & Schaffner-Bielich, J. 2012b, PhRvC, 85, 065802
Yamamoto, Y., Furumoto, T., Yasutake, N., & Rijken, T.A. 2013, PhRvC, 88, 022801